01 Sep 2011

Γ-CT Measurement and CFD Simulation of Cross Section Gas Holdup Distribution in a Gas-Liquid Stirred Standard Rushton Tank

Yue Jin Liu

Wei Li

Lu Chang Han

Yang Cao

et. al. For a complete list of authors, see https://scholarsmine.mst.edu/che_bioeng_facwork/1271

Recommended Citation

Y. J. Liu et al., "Γ-CT Measurement and CFD Simulation of Cross Section Gas Holdup Distribution in a Gas-Liquid Stirred Standard Rushton Tank," *Chemical Engineering Science*, vol. 66, no. 17, pp. 3721 - 3731, Elsevier, Sep 2011.

The definitive version is available at https://doi.org/10.1016/j.ces.2011.03.042

Chemical Engineering Science 66 (2011) 3721–3731

Contents lists available at ScienceDirect

Chemical Engineering Science

journal homepage: www.elsevier.com/locate/ces

Review

γ-CT measurement and CFD simulation of cross section gas holdup distribution in a gas–liquid stirred standard Rushton tank

Yue-Jin Liu [a,*], Wei Li [a], Lu-Chang Han [a], Yang Cao [a], He-an Luo [a], Muthanna Al-Dahhan [b], M.P. Dudukovic [b]

[a] School of Chemical Engineering, Xiangtan University, Xiangtan 411105, China
[b] Chemical Reaction Engineering Laboratory, Washington University in St. Louis, MO 63130, USA

ARTICLE INFO

Article history:
Received 1 September 2010
Received in revised form
16 March 2011
Accepted 18 March 2011
Available online 2 April 2011

Keywords:
Gas holdup distribution
γ-CT measurement
Rushton tank
Larger gas flow
CFD simulation

ABSTRACT

Cross section gas holdup distributions at 3/4 dimensionless static liquid height in a gas–liquid stirred standard Rushton tank were measured using ^{137}Cs γ-CT scan measuring technology at larger gas flow rates and higher impeller rotating speeds. The obtained CT scan images and digital distribution curves of gas holdup with dimensionless radius based on the CT images could explain the fluctuation changes of gas holdup distribution. The dense area of gas holdup distribution appeared in the upper space of impeller blades. Gas holdup increased both with gas flow rate and impeller rotating speed, but gas flow rate had more influence on gas holdup than impeller rotating speed. The Eulerian–Eulerian two-fluid model coupling with the bubbles' coalescence and break-up models, and the drag coefficient model were established to make CFD simulation of gas holdup distributions for the gas–liquid stirred Rushton tank under different gas flow rates and impeller rotating speeds.

Contents

1. Introduction

Gas–liquid stirred Rushton tanks were widely used in industries, such as the petrochemical, paper and pulp, pharmaceutical, fine chemicals, food industries, etc. Gas holdup and its distribution

* Corresponding author.
E-mail address: xdlyj@163.com (Y.-J. Liu).
0009-2509/$ - see front matter © 2011 Elsevier Ltd. All rights reserved.
doi:10.1016/j.ces.2011.03.042

were the most essential characteristics of gas–liquid stirred Rushton tank, as they determined the contact area between gas and liquid phases. However, the determinations of gas holdup and its distribution in gas–liquid stirred Rushton tank were still regarded among the most difficult topics to tackle (Venneker et al., 2002; Hristov et al., 2008).

There were some measuring techniques of gas holdup, but most of them were limited to point or local measurement in transparent system (Chaouki et al., 1997; Boyer et al., 2002; Wang, 2002; Bao et al., 2010). Based on the radiation and digital image technology, cross section void fraction distributions in gas–liquid or gas–solid two phases were measured using γ-ray or X-ray CT (computer tomography) scan measuring technique (Kumar et al., 1995, 1997; Chen et al., 1999; Kemoun et al., 2001; Dudukovic, 2002; Khopkar et al., 2005; Ford et al., 2008). There were no limitations of the opacity, high concentration, high temperature and high pressure for measured systems and it was a non-invasive measuring technology.

Rammohan (2002) had successfully scanned a gas–liquid stirred standard Rushton tank with ^{137}Cs γ-ray CT scan measuring technique. However, they met a mechanical vibration problem with the shaft that connected a motor and an impeller, when impeller rotated at higher speed. So the maximal impeller rotating speed was set at 400 rpm, and subsequently, the corresponding maximal gas flow rate could only be set at 7.5 L min^{-1}. Otherwise, the flood phenomenon or cup dispersion states of gas in liquid (Nienow, 1977; Alessandro et al., 2000; Wang et al., 2006; Liu et al., 2006) would occur, which was the worst gas dispersion state and should be avoided from appearing.

In this work, after the mechanical vibration problem of the shaft had been solved, ^{137}Cs γ-ray CT scan measuring experiments for a gas–liquid stirred standard Rushton tank were successfully done at larger gas flow rates and higher impeller rotating speeds, when gas dispersion states exceeded their corresponding critical gas dispersion states or load states (Nienow et al., 1977; Paglinanti et al., 2000; Wang et al., 2006; Liu et al., 2006). And the cross section CT images of gas holdup distribution and their corresponding digital distribution curves with dimensionless radius were obtained.

In addition, there were some CFD simulation works on gas holdup or gas holdup distribution for the gas–liquid stirred Rushton tank. In such literatures, an Eulerian–Eulerian two-fluid model along with the standard k–ε turbulence model was used to simulate the dispersed gas–liquid flow in a Rushton stirred-tank. Appropriate drag corrections to account for bulk turbulence were developed to correctly simulate different flow regimes (Ranade and Deshpande, 1999; Ranade et al., 2001; Lane et al., 2002, 2005; Khopkar et al., 2005; Zhang et al., 2009). In contrast, Han et al. (2007) used the discrete particle method coupling with the k–ε turbulence model to simulate the axial distribution of gas holdup. Ranade and Deshpande (1999) and Ranade et al. (2001) had simulated gas–liquid flow by extending a computational snapshot approach, which obtained contours of gas holdup distribution at impeller center plane. Many of them were restricted to low gas flow rate within the complete dispersion regime. Lane et al. (2002, 2005) had proposed a new method for calculating drag coefficient, which took into account the effect of interaction between bubbles and turbulent eddies, and the simulation work had been carried out to predict gas holdup distributions at higher gas flow rate. Khopkar et al. (2005) obtained cross section images of gas holdup distribution at higher gas flow rate using the Eulerian–Eulerian two-fluid model along with the standard k–ε turbulence model, but the predicted results showed a low resolution ratio compared with the experimental measured CT images.

In this work, the Eulerian–Eulerian two-fluid model along with the standard k–ε turbulence model was used to simulate the dispersed gas–liquid flow. The drag correction model to account for turbulence was used to simulate both the inner-stirred region and non-stirred regions. The bubble coalescence and break-up models were used to simulate bubbles' size. The Multiple Frames of Reference approach was used to simulate the impeller rotation regime and the SIMPLEC algorithm was used to solve the items of velocity and pressure. The upwind finite difference scheme was used to disperse the convective terms and diffusion terms in the continuity equation. Three-dimensional CFD simulations for the gas–liquid stirred Rushton tank were carried out to get the distributions of gas holdup. The comparison and discussion of the CFD simulated gas holdup distributions with the CT measured results were performed.

2. Experimental apparatus

The experimental apparatus consisted of two parts. One part was a gas–liquid stirred standard Rushton tank and another part was a 100 mCi ^{137}Cs γ-CT setup.

A gas–liquid stirred standard Rushton tank was of ∅20 cm × 24 cm with 20 cm static liquid height. Four baffles of 1.6 cm width were mounted perpendicular to the wall of tank. The impeller was a disk of 5 cm diameter with six blades of 17 cm × 13 mm symmetrically inserted into 8.5 mm, and it was located at 1/3 dimensionless static liquid height and linked with a shaft of 8 mm diameter. A ring sparger of 6.66 cm diameter with 8 holes was set at 1 cm away from the bottom of tank.

In this study, the experimental operation conditions were listed as Table 1 based on the flow number ($Fl=Q_G/ND_I^3$, the ratio of the sparger rate of gas to the rate of pumped liquid) and the Froude number($Fr=N^2D_I/g$, the ratio of inertial or centrifugal force of moving-tangentially outward liquid near the edge of rotating impeller to the gravitational force).

The support structure of the CT setup consists of four threaded vertical guide rods on which a perfectly horizontal plate was positioned so as to allow its smooth vertical motion automated by gears. On this a gantry plate was fixed. The gantry plate houses the 100 mCi lead shielded Cs-137 source and an array of seven NaI (Tl) detectors, which were positioned across the vessel diameter facing the source. The whole assembly (source plus detector array) rotated around the vessel during the data acquisition process. Thick lead shielding in front of the source was used to collimate the radiation into a fan beam whose angle can be varied to envelop the vessel. The detector array also has a lead collimator that can move, controlled by a stepper motor, in front of the detector (Fig. 1).

The whole experimental measuring setup was illustrated in Fig. 2. More details of the measuring and imaging principle related references (Kumar et al., 1995; Rammohan, 2002).

Table 1
Experimental conditions.

Gas rates, L min^{-1}	Impeller speeds, rpm		
9.44	350[a] (Fl=0.09, Fr=0.23)	500 (Fl=0.06, Fr=0.47)	800 (Fl=0.04, Fr=1.21)
18.88	470[a] (Fl=0.14, Fr=0.42)	600 (Fl=0.11, Fr=0.68)	800 (Fl=0.08, Fr=1.21)
28.32	530[a] (Fl=0.18, Fr=0.53)	640 (Fl=0.15, Fr=0.77)	800 (Fl=0.12, Fr=1.21)

[a] Critical impeller speeds.

3. CT scan measuring experiments

3.1. Experimental conditions

The purpose of this section was to measure, compare and analyze gas holdup distributions under different gas flow rates and impeller rotating speeds, when gas dispersion states exceeded their corresponding critical dispersion states. However, even when gas dispersion states exceeded their corresponding critical dispersion states, gas holdup distributions in the gas–liquid stirred Rushton tank were not uniform both in axial and in radius directions. There were developing and developed regions along axial direction above the plane of impeller. The developed stable regions of cross section gas holdup distribution appeared at about 3/4 dimensionless static liquid height (see Section 3.3.4), so the CT scan measuring location was set at this height.

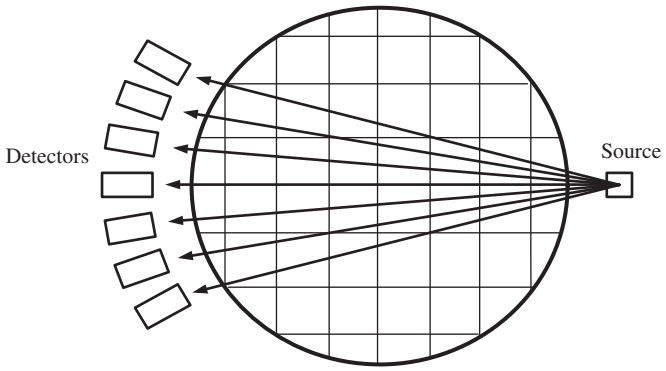

Fig. 1. Sketch of γ-CT scan.

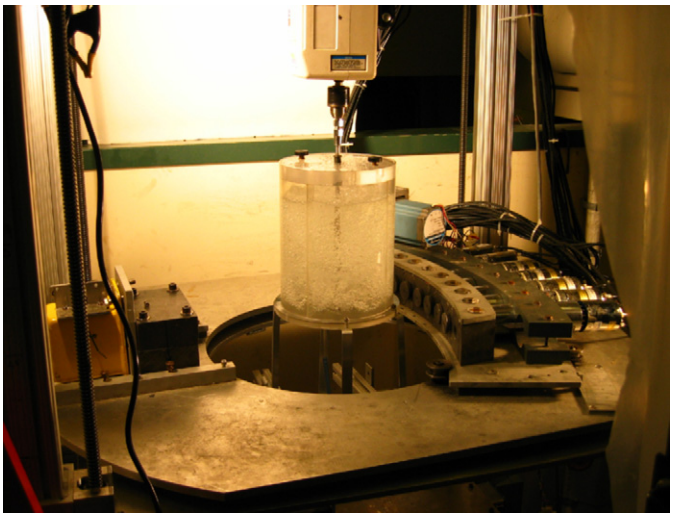

Fig. 2. Experimental measuring setup of γ-CT.

Although there was a cover at the top of tank with some holes, if gas flow rate exceeded 28.32 L min^{-1} (60SCFH), liquid in tank was easy to be entrained out by gas. Under a given gas flow rate, when impeller rotating speed gradually increased from zero, gas dispersion state in liquid could be divided into three states based on our experimental observation: (a) cup dispersion, (b) critical dispersion, and (c) full dispersion as illustrated in Fig. 3, which was somewhat different from the division of five gas dispersion states presented in literatures (Nienow et al., 1977; Wang et al., 2006). Especially, the discovery of critical dispersion process that looked like completely opening an umbrella from a half-opening state (cup dispersion) was very important, and it was an obvious division between cup dispersion and full dispersion. So gas flow rate was set at 9.44 L min^{-1} (20SCFH), 18.88 L min^{-1} (40SCFH) and 28.32 L min^{-1} (60SCFH), and their corresponding critical impeller speeds were determined as 350, 470 and 530 rpm, respectively. If impeller rotating speed exceeded 800 rpm, both the vibrations of both the shaft and the tank, and the inhalation of air through holes of top cover of tank would take place. In order to examine full dispersion behavior under an extreme state, the highest impeller rotating speed was set at 800 rpm. The experimental conditions were listed in Table 1.

3.2. CT scan images

Because the gap of CT detectors to receive radiation signal from the source was 2 mm × 2 mm, the resolution of CT instrument to receive radiation signal was 2 mm × 2 mm. Thereby, each pixel unit of measured object cross-section was 2 mm × 2 mm too. The error bar associated with the CT measurement is ±0.02, while the radius R changed from 0 to 100 mm.

Under the above experimental conditions listed in Table 1, ^{137}Cs γ-CT scan measuring experiments for the air–water stirred standard Rushton tank at 3/4 dimensionless static liquid height were performed. The obtained CT images of gas holdup distribution were illustrated in Figs. 4–6.

From Figs. 4–6, it could be seen that the obtained CT scan images could clearly demonstrate the cross section gas holdup distributions and their changes. The dense area of gas holdup distribution appeared in the upper space of impeller blades, and gas holdup increased with both gas flow rate and impeller rotating speed. For more detailed information about the gas

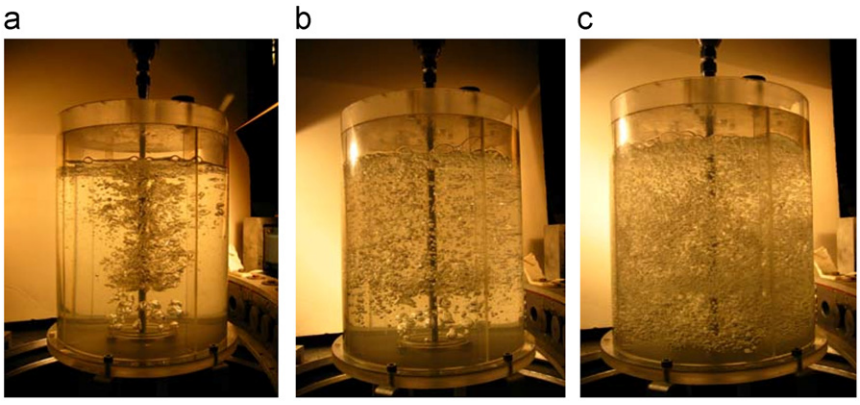

Fig. 3. Three gas dispersion stages: (a) cup dispersion; (b) critical dispersion; (c) full dispersion.

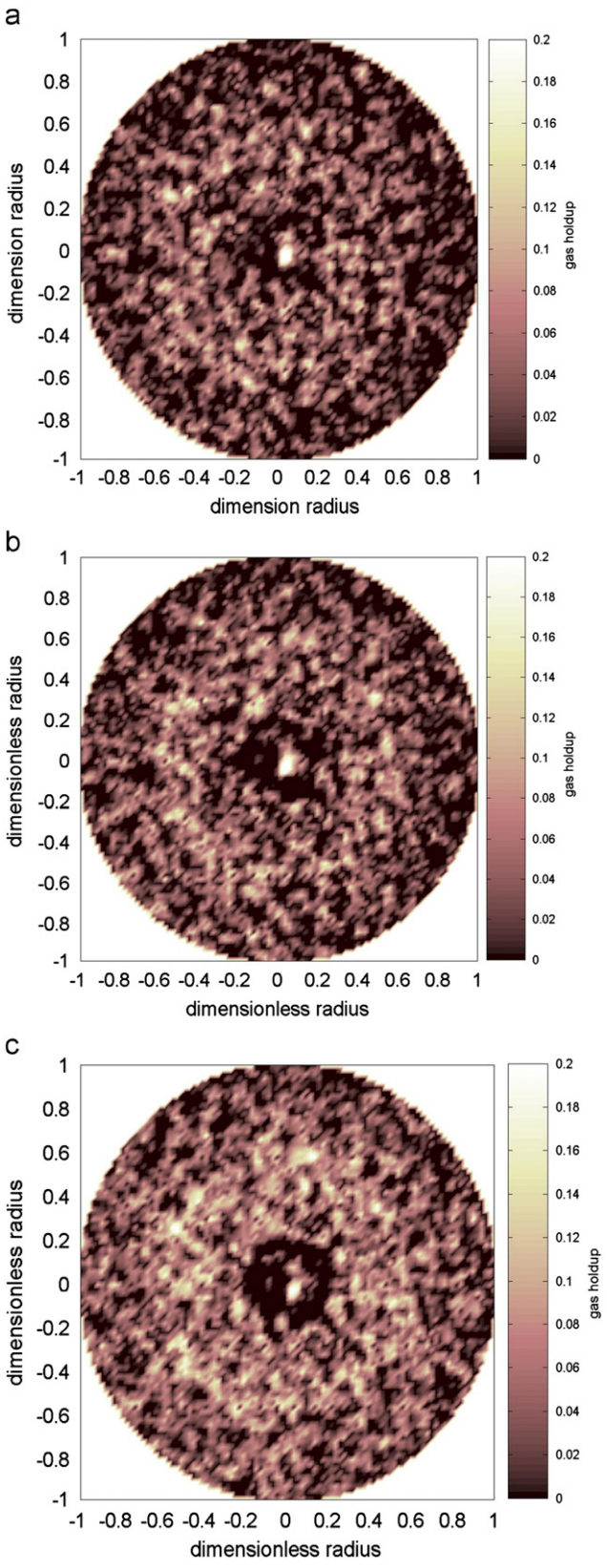

Fig. 4. CT images of gas holdup distribution with gas flow rate 9.44 L min^{-1} and impeller rotating speeds: (a) 350 rpm, (b) 500 rpm and (c) 800 rpm.

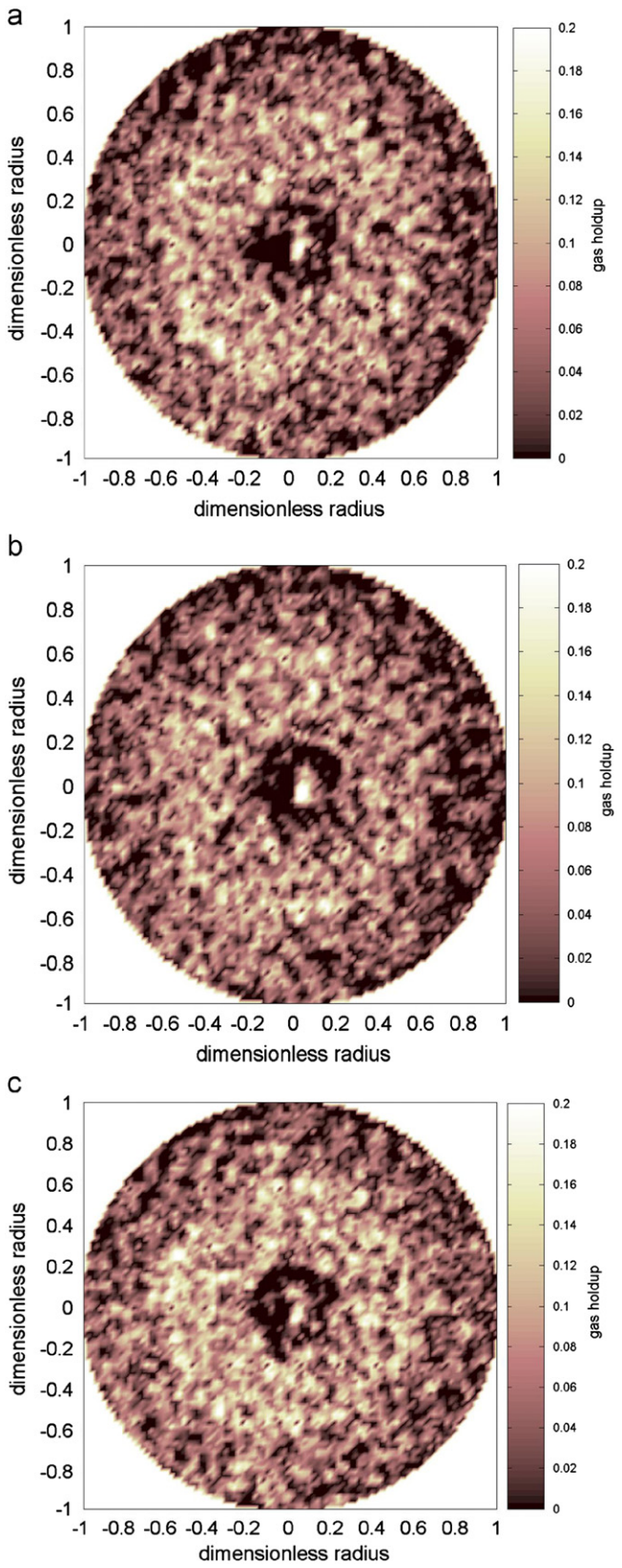

Fig. 5. CT images of gas holdup distribution with gas flow rate 18.88 L min^{-1} and impeller rotating speeds: (a) 470 rpm, (b) 600 rpm and (c) 800 rpm.

holdup distributions and their changes, the digital distribution curves of gas holdup with dimensionless radius based on the CT scan images should be further examined.

3.3. Digital distribution curves

In general, CT scan image is only a qualitative description, while digital distribution curve is a quantitative expression of CT

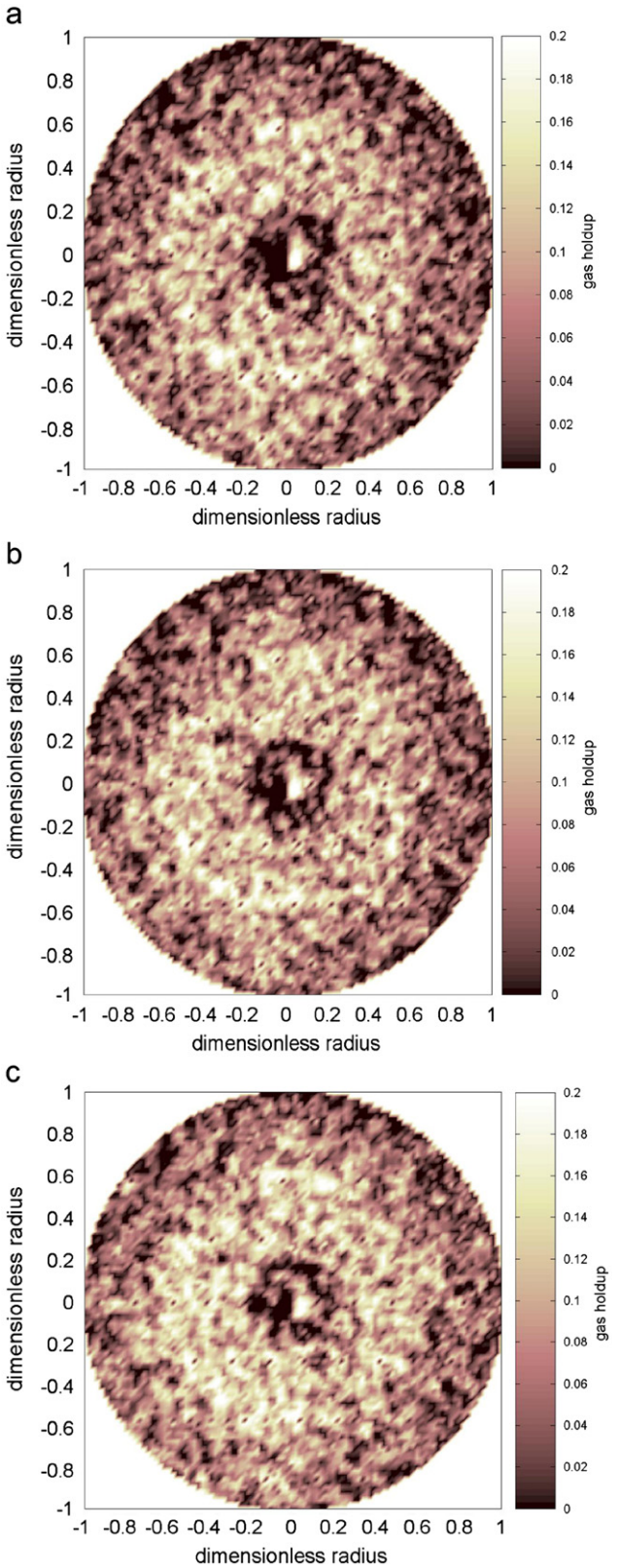

Fig. 6. CT images of gas holdup distribution with gas flow rate 28.32 L min^{-1} and impeller rotating speeds: (a) 530 rpm, (b) 640 rpm and (c) 800 rpm.

scan image. It can be obtained to average radial gas holdup based on CT measurement data in this way that gas holdup corresponded all pixels along a circle at given radius was summed and then was divided by the number of passed pixels. Figs. 7–10 were

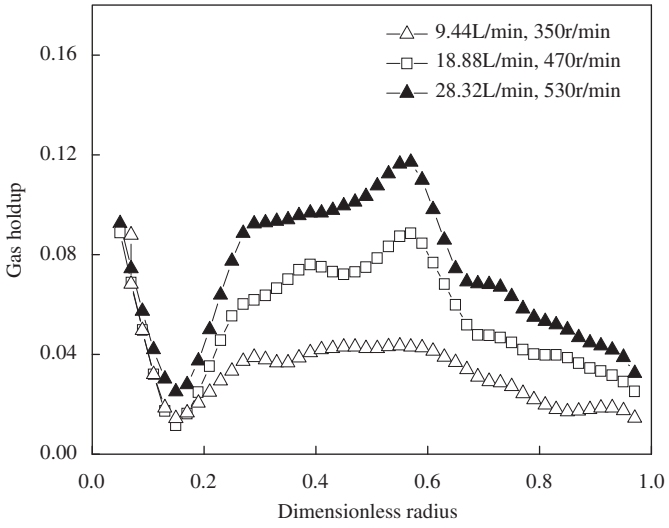

Fig. 7. Digital distribution curves of gas holdup at three critical gas dispersion states.

called digital distribution curve relative to CT scan image, which is more convenient for us to analyze and to compare CT measurement results quantitatively.

3.3.1. *Three critical gas dispersion states*

The digital distribution curves of gas holdup with dimensionless radius at three critical gas dispersion states were illustrated in Fig. 7.

It was clear that, from Fig. 7, although gas dispersion states had reached the critical gas dispersion states, there were larger fluctuations of gas holdup distribution with dimensionless radius and all the fluctuations almost had the similar shapes—first experiencing a concave peak and then a convex one. The detailed descriptions were as follows.

First, gas bubbles were easy to yield and be adsorbed on the rough surface of rotating shaft (0.08 d.r.), so more gas bubbles appeared here. Then, gas holdup sharply decreased to the lowest at about 0.18 d.r., it was because that gas bubbles rising from the ring sparger (0.315 d.r.) were obstructed by the disk (0.25–0.335 d.r. plus blade) of impeller. In this range, there was almost the same declining track for three critical gas dispersion states, which meant that both gas flow rate and impeller rotating speed had little influence on gas holdup distribution.

When dimensionless radius increased from 0.18 to 0.3, gas holdup increased sharply. It was because the gas bubbles rising from the sparger were broken into smaller pieces by six rotating blades of impeller and part of them rose towards the center area, while most of them were forced to move outwards under the action of centrifugal force of pumped liquid by rotating impeller. Gas holdup increased plainly when dimensionless radius was in the range of 0.3–0.58, especially at 9.44 L min^{-1} of gas flow rate. The larger the gas flow rate was, the more the gas holdup increased.

When dimensionless radius was in the range of 0.58–0.65, gas holdup declined steeply. It was because of that the outward-moving of gas bubbles became gradually weakened with the increasing of dimensionless radius, due to the friction between the outward-moving bubbles and the pumped liquid. However, when dimensionless radius was in the range of 0.65–1, this declining tendency of gas holdup did not keep so steeply. It was because there was a circling-liquid flow between the central region (moving down) and the near-wall region (moving up),

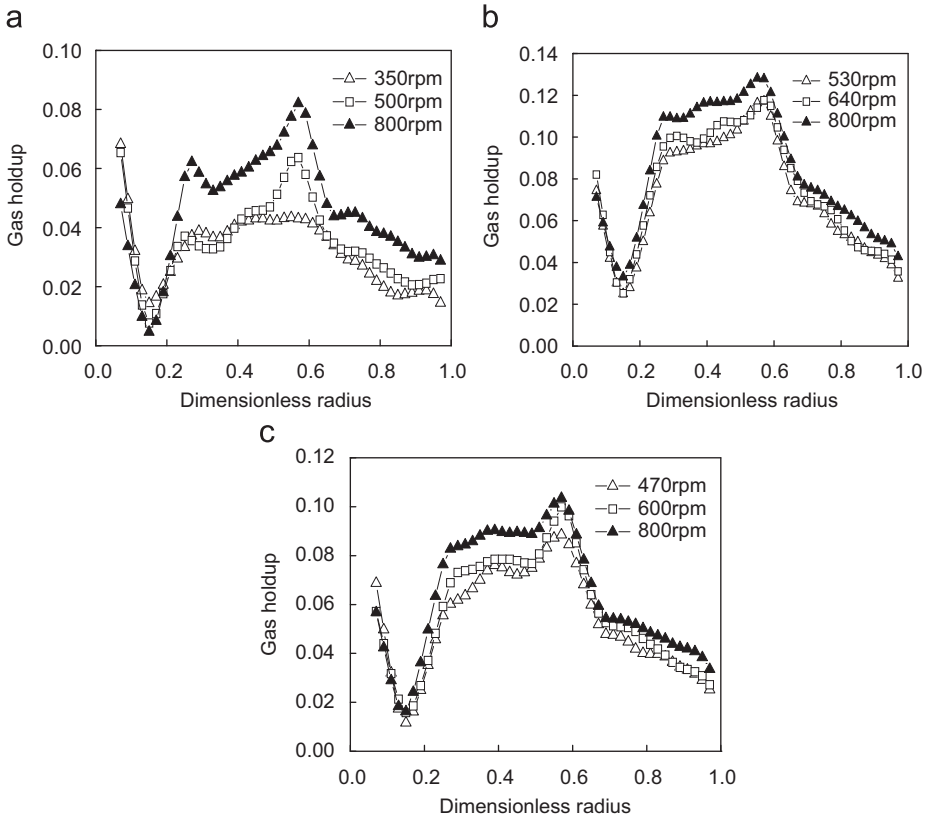

Fig. 8. Effect of impeller rotating speed on gas holdup distribution at three gas rates: (a) 9.44 L min^{-1}, (b) 18.88 L min^{-1} and (c) 28.32 L min^{-1}.

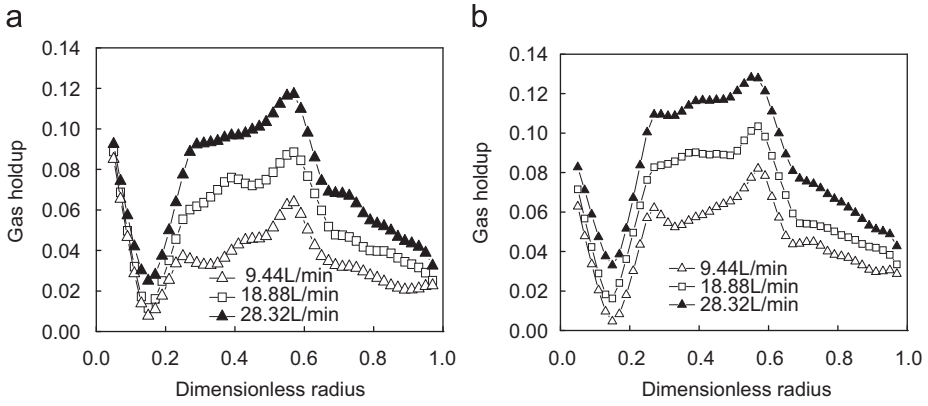

Fig. 9. Effect of gas flow rate on gas holdup distribution at two impeller rotating speeds: (a) 500 rpm and (b) 800 rpm.

and the moving-up flow of near-wall region with some gas bubbles made up for a little of gas holdup.

Also, it was easy to note that at the critical state of gas flow rate 9.44 L min^{-1}, the fluctuant change of gas holdup with dimensionless radius appeared a little bit plain when dimensionless radius exceeded 0.25, compared with other two distributions of gas holdup in this range.

3.3.2. *Effect of impeller rotating speed*

The effect of impeller rotating speed on gas holdup distribution was illustrated in Fig. 8.

From Fig. 8, it could be seen that, there was almost the same concave peak of gas holdup, when dimensionless radius was in the range of 0.08–0.25. It meant that impeller rotating speed had little effect on gas holdup in this range. Gas holdup increased a little with the increasing of impeller rotating speed, only when dimensionless radius was between 0.25 and 0.6. However, at 9.44 L min^{-1} of gas flow rate and 800 rpm of impeller rotating speed, gas holdup had larger increase with impeller rotating speed than other two bigger gas flow rates, when dimensionless radius exceeded 0.25.

3.3.3. *Effect of gas flow rate*

The effect of gas flow rate on gas holdup distribution was illustrated in Fig. 9.

It could be seen, from Fig. 9, that whether impeller rotating speed was 500 or 800 rpm, except in the range of 0.08–0.25 d.r., gas holdup increased obviously with the increasing of gas flow rate, especially in the range of 0.25–0.6 d.r. This meant that, compared with Fig. 8, gas flow rate had more effect on gas holdup than impeller rotating speed.

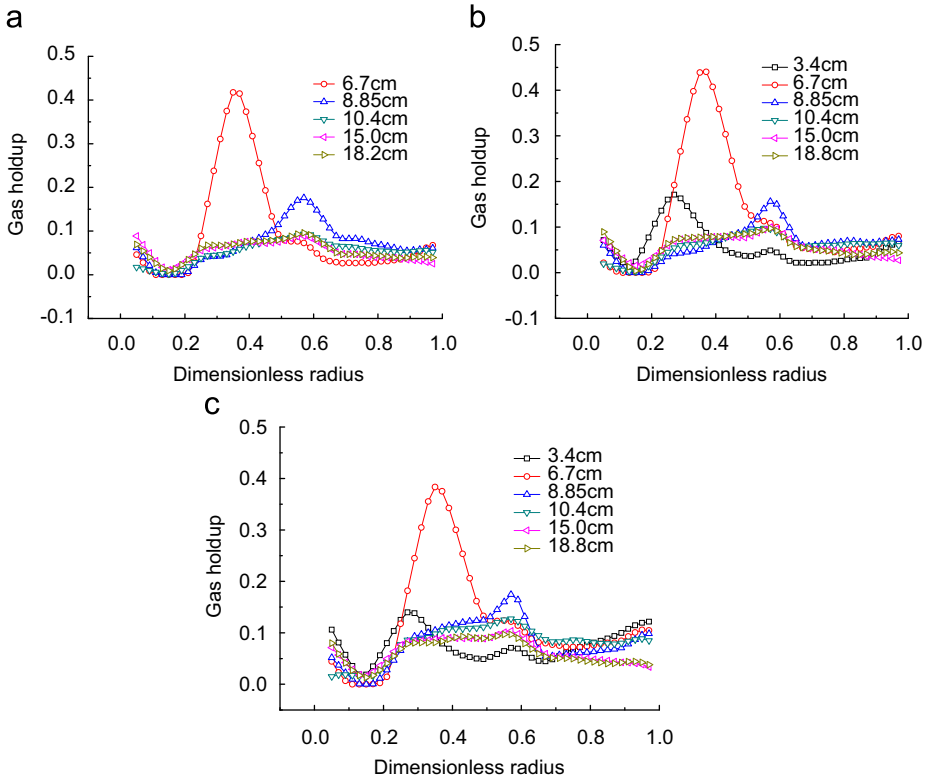

Fig. 10. Gas holdup distribution on different cross section at three impeller rotating speeds: (a) 470 rpm, (b) 600 rpm and (c) 800 rpm.

Through the above analyses of CT scan measuring results, including both the images and the digital curves of gas holdup distribution and the related discussions, we could conclude that gas holdup distribution in the gas–liquid stirred Rushton tank was first subjected to the configuration of Rushton tank, and then gas holdup increased both with gas flow rate and impeller rotating speed, but gas flow rate had more effect on gas holdup than impeller rotating speed after critical gas dispersion state.

3.3.4. *Effect of different cross sections*

Gas holdup distributions at different cross sections with different impeller rotating speeds at the same gas flow rate 18.88 L min^{-1} were shown in Fig. 10. The tendency of gas holdup distribution along dimensionless radius at different cross sections was roughly the same except for at the height of impeller blade. There was a remarkable change of cross section gas holdup at the height of impeller blade (6.7 cm), and a slight variation below impeller blade (3.4 cm) compared to the location of impeller blade. Above the location of impeller blade, the change of cross section gas holdup became small with increase in dimensionless static liquid height. When static liquid height exceeded at 10.4 cm, there was also a little change. It showed a comparative uniform distribution of gas holdup distribution, so the CT scan measuring location was set at 3/4 dimensionless static liquid height (the middle cross section among 10.4, 15.0 ,18.8 cm).

4. CFD simulation

4.1. *Mathematical models*

The Eulerian–Eulerian two-fluid model along with the standard k–ε turbulence model was used to simulate the dispersed gas–liquid flow. The drag correction model to account for turbulence was used to simulate the inner-stirred region and non-stirred regions.

Table 2
Main items and corresponding options.

Items	Options
Drag coefficient	Schiller and Naumann drag Model
Added mass force coefficient	$C_{vm}=0.52$
Bubble break-up	Luo and Svendsen Model
Bubble coalescence	Prince and Blanch Model
MUSIG model	20 bubble classes; $d_{min}=0.1$ mm, $d_{max}=10$ mm

The models of bubble coalescence and breakage were used to simulate bubbles' size. The Multiple Frames of Reference approach was used to simulate the impeller rotation regime, and the SIMPLEC algorithm was used to solve the items of velocity and pressure. The upwind finite difference scheme was used to disperse the convective terms and diffusion terms in continuity equation. In this way, the CFD models were established to simulate gas holdup distribution in the gas–liquid stirred Rushton tank. The main items and corresponding options in the CFD models were listed in Table 2.

The continuity equation was

$$\frac{\partial(\alpha_k\rho_k u_k)}{\partial t}+\nabla\cdot(\alpha_k\rho_k u_k)=S_k \tag{1}$$

where the subscript k denoted phase and S_k as a source term of phase k.

The motion equation was

$$\frac{\partial(\alpha_k\rho_k u_k)}{\partial t}+\nabla\cdot(\alpha_k\rho_k u_k)=-\alpha_k\nabla p+\alpha_k\rho_k g+F_T\pm F_{int} \tag{2}$$

here F_T and F_{int} respectively represented the stress tensor in phase k, and the interaction forces between gas–liquid two phases, such as drag force, lift force and added mass force. The MUSIG simulation was performed with equant 20 classes of bubble diameter from 0.1 to 10 mm. The bubbles were not uniformly distributed by bubble

class, the spatial distributions of bubble size in connection with turbulent dispersion. It was based on collision frequency between a particle of size di and eddies of a size between de and de+d(de), but the expression for the velocity and number density of eddies is slightly different. The following equation was used to calculate the collision frequency:

$$\Omega(V_i,V_j)=\int_0^{\infty} w(d_i,d_e)P_b(d_i,d_j,d_e)d(d_e) \tag{3}$$

4.1.1. Drag coefficient

The drag coefficient was important hydrodynamic parameter involved in modeling, which had to be provided as input data (Brucato et al., 1998; Han et al., 2007), and had great influence on gas holdup distribution. Schiller and Naumann drag coefficient model was applicable to gas–liquid system of low gas holdup (Law et al., 2008). The interactions among gas bubbles also enhanced with gas holdup increased. The drag coefficient correlation employed as (Brucato et al., 1998)

$$\begin{cases} C_D=\frac{24}{Re_b}(1+0.15Re_b^{0.687}), & Re_b<1000 \\ C_D=0.44, & Re_b\geq 1000 \end{cases} \tag{4}$$

4.1.2. Break-up model

In gas–liquid stirred Rushton tank, bubbles broken-up caused mainly by turbulent eddy collision. Luo and Svendsen (1996) model based on gas dynamics theory assumed that turbulence was isotropic and all the bubbles were binary broken-up, and had successfully explained that the broken-up rate was equal to the product of the bubble turbulent frequency of eddy collision and the broken-up efficiency. The break-up rate of bubble volume V_j by turbulent dissipation broken into V_i was (Luo et al., 1996; Liao et.al., 2009)

$$g(V_j:V_i)=f_B 0.923(1-\alpha_G)\left(\frac{\varepsilon}{d_j^2}\right)^{1/3}\int_{\xi_{\min}}^{1}\frac{(1+\xi)^2}{\xi^{11/3}}\exp\left(-\frac{12c_f\sigma}{\beta\rho_c\varepsilon^{2/3}d^{5/3}\xi^{11/3}}\right)d\xi \tag{5}$$

where, $\xi_{min}=11.4\lambda/d_i$ and λ was the micro-scale of Kolmogorov, $\lambda=(V_L^3/\varepsilon)^{1/4}$; V_L was the kinematic viscosity, ε the turbulence dissipation rate, σ the surface tension of continuous phase; c_f was the increase coefficient of surface area, expressed as $0\leq c_f=f_v^{2/3}+(1-f_v)^{2/3}-1\leq 0.26$, and $f_v=d_i^3/d^3$.

Therefore the growth rate of new bubble group i generated by big bubbles' broken-up was calculated by the following equation:

$$B_B=\sum_{j=j+1}^{N} g(V_j:V_i)n_j \tag{6}$$

4.1.3. Coalescence model

The coalescence process of gas bubbles was simulated by the collision frequency and the coalescence rate between two bubbles. The collision frequency and coalescence rate associated with the contact time τ_{ij} and coalescence time t_{ij}, respectively. The Prince and Blanch (1990) model was employed. Prince and Blanch considered that bubble coalescence was likely caused by turbulence, buoyancy and laminar shear forces. The coalescence rate was

$$C_{ij}=F_C\left(\theta_{ij}^T+\theta_{ij}^B+\theta_{ij}^{LS}\right)\eta_{ij} \tag{7}$$

$$\eta_{ij}=e^{(-t_{ij}/\tau_{ij})} \tag{8}$$

$$t_{ij}=\left(\frac{r_{ij}^3\rho_L}{16\sigma}\right)\ln\frac{h_0}{h_f} \tag{9}$$

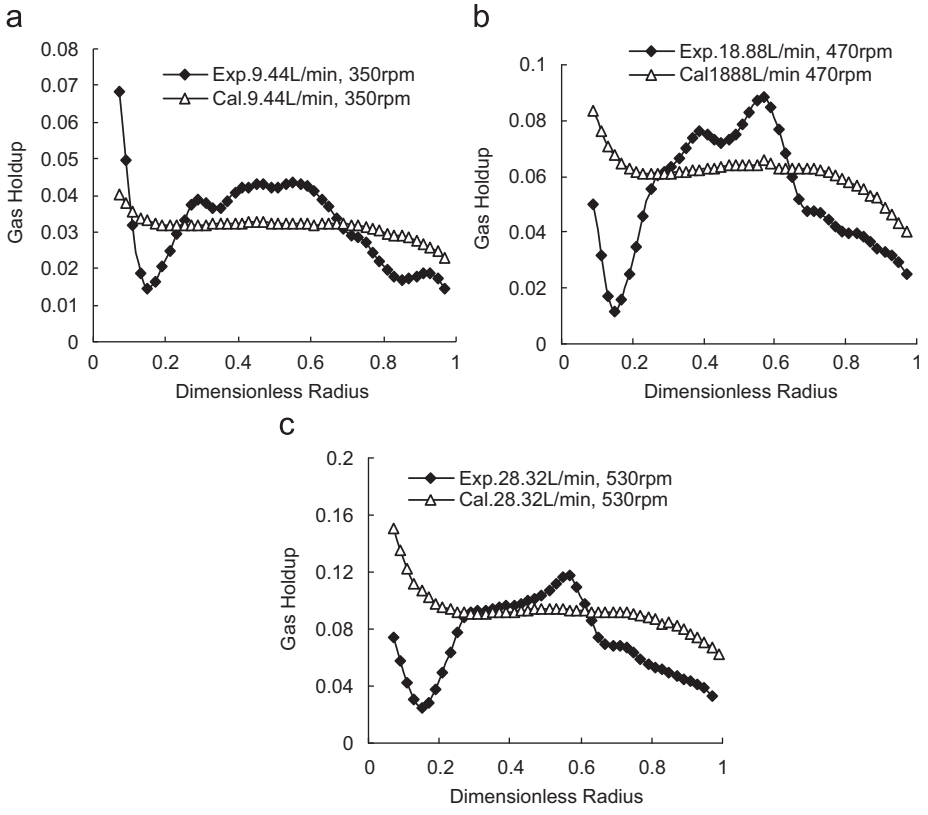

Fig. 11. Comparison of CFD simulated values with CT measured results of gas holdup distributions at three critical gas dispersion states.

$$\tau_{ij} = \frac{r_{ij}^{2/3}}{\varepsilon^{1/3}} \tag{10}$$

In Eq. (7), F_C was the correction coefficient,η_{ij} the probability of bubble coalescence, h_0 the initial film thickness, h_f the critical thickness of film rupture, r_{ij} the radius. The equivalent radius needed for the coalescence of unequal-sized bubbles was calculated from

$$r_{ij} = \frac{1}{2}\left(\frac{1}{r_i} + \frac{1}{r_j}\right)^{-1} \tag{11}$$

$$\theta_{ij}^{T} = S_{ij}(u_{ti}^2 + u_{tj}^2)^{1/2} \tag{12}$$

where, S_{ij} was the contact area of two bubbles, $S_{ij} = \pi/4(d_i + d_j)^2$; u_{ti} was the bubble turbulence velocity, $u_{ti} = \sqrt{2}\varepsilon_L^{1/3} d_i^{1/3}$.

When group j bubbles and group k bubbles coalesced, new group i bubbles generated, and the coalescence rate was as follow

$$B_C = \frac{1}{2}\sum_{j=1}^{i}\sum_{k=1}^{i} Q_{jk} n_j n_i \tag{13}$$

4.1.4. Boundary conditions

Considering the symmetry of geometry, one sixth of tank was considered as a computational domain. And the inner stirred region was radically positioned at 0 m $\le r \le$ 0.06 m and axially at 0.04 m $\le z \le$ 0.12 m.

Bubbles escaped into liquid phase through 8 holes of the ring sparger and the sparger was modeled as a solid wall. All walls were treated as non-slip boundaries using their corresponding standard wall functions, and the top surface of liquid was treated as zero gradient of boundary. The ring sparger holes' surfaces were considered as the inlet area for determining gas velocity (Khopkar et al., 2008), and the axial outgoing velocity of gas bubbles was equal to the terminal rise velocity of bubbles (Khopkar et al., 2005). The freedom-slip boundary condition was used for liquid phase and the non-slip boundary condition for gas phase.

The SIMPLE algorithm was used to solve the pressure field from the continuity equation, and an upwind finite difference scheme was used to disperse the convective terms and diffusion terms in the continuity equation, anisotropic momentum equation, Reynolds stress model, turbulent kinetic energy and the rate of turbulent dissipation transport equations. Then, the second-relaxation iterative method was used to solve governing equation point by point. The computation was considered converged when the normalized residuals of each primary variable dropped below 10^{-5}.

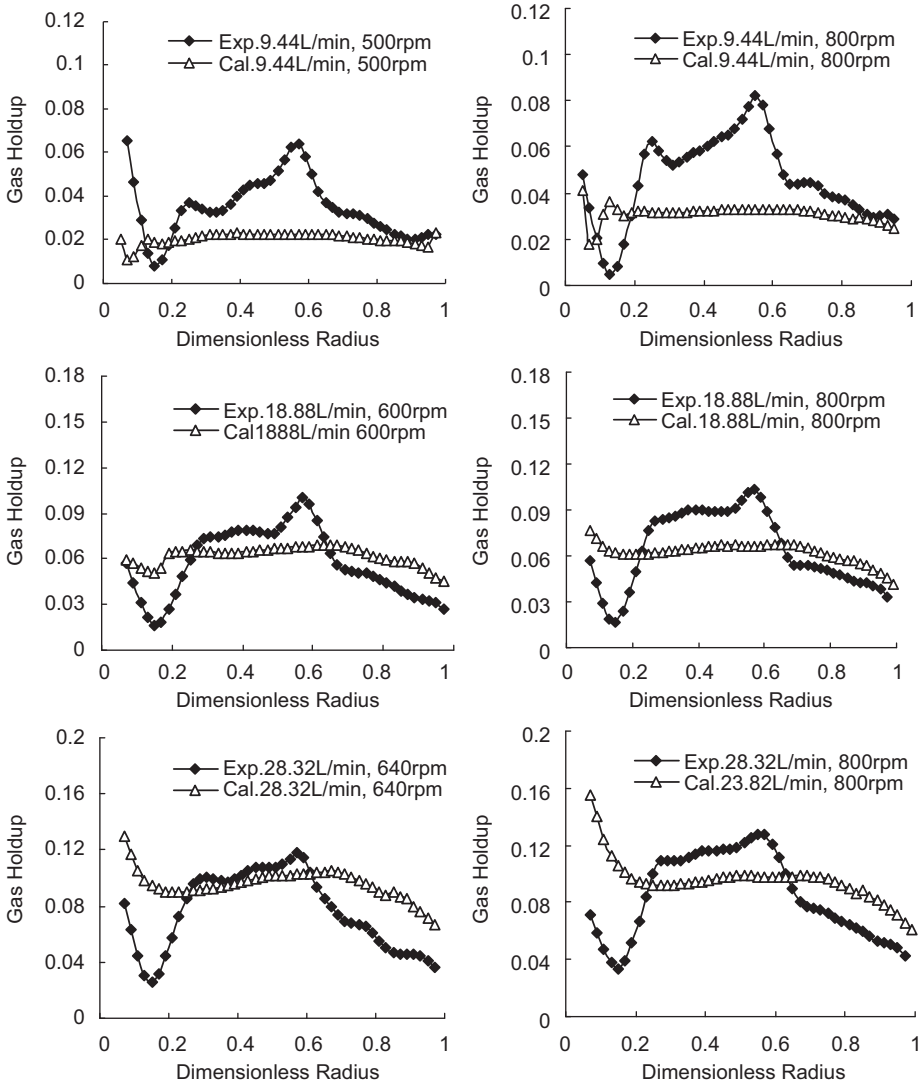

Fig. 12. Comparison of CFD simulated with CT measured values with different gas flow rates and impeller rotating speeds.

4.2. Simulated results and discussion

4.2.1. Three critical gas dispersion states

The CFD simulated values with the CT measured results of cross section gas holdup distributions at 3/4 dimensionless static liquid height in the gas–liquid stirred Rushton tank at three critical gas dispersion states were illustrated in Fig. 11.

From Fig. 11, it could be seen that, on the whole, the CFD simulated gas holdup distributions with dimensionless radius were roughly similar to the CT measured results at three critical gas dispersion states. When gas flow rate was 9.44 L min^{-1}, the CFD simulated gas holdup distribution was averagely closer to the CT measured results, but when gas flow rate increased, the CFD simulated gas holdup values became larger than the CT measured results, i.e. the whole CFD simulated distribution curves of gas holdup with dimensionless radius were upward away from those of the CT measured results.

Near the axial region, the CFD simulated gas holdup values sharply decreased with the increasing of dimensionless radius, and these declining trends somewhat approached those of the CT measured results, except at 9.44 L min^{-1} of gas flow rate. In the middle region, the CFD simulated gas holdup distributions were very smooth, which could not reflect the fluctuation changes of the CT measured results. Near the tank-wall region, the CFD simulated gas holdup values gradually decreased with the increase in dimensionless radius, these declining trends approached the CT measured results, although the CFD simulated values were larger than the CT measured results in this region.

4.2.2. Effects of gas flow rate and impeller rotating speed

The CFD simulated values with the CT measured results of cross section gas holdup distributions at 3/4 dimensionless static liquid height in the gas–liquid stirred Rushton tank at different gas flow rates and impeller rotating speeds were illustrated in Fig. 12.

On the whole, from Fig. 12, the CFD simulated gas holdup distributions with dimensionless radius were similar to the critical gas dispersion rates illustrated in Fig. 11. Near the axial area, when gas flow rate was lower, there was a very small CFD simulated concave peak of gas holdup distribution, which could somewhat reflect a little change of the CT measured results. When gas flow rate increased, no CFD simulated concave peak could appear. The CFD simulated gas holdup values increased both with the increase in gas flow rate and impeller rotating speed. The CFD simulated gas holdup values were more influenced by gas flow rate than by impeller rotating speed, which reflected the same effect of the CT measured results.

5. Conclusions

Under larger gas flow rates and higher impeller rotating speeds, the cross section gas holdup distributions at 3/4 dimensionless static liquid height in the gas–liquid stirred standard Rushton (20 cmi.d.) were measured using ^{137}Cs γ-CT scan technology, when gas dispersion states exceeded the critical gas dispersion states. The obtained CT scan images could clearly demonstrate the cross section gas holdup distributions and their changes. The dense area of gas holdup distributions appeared in the upper space of impeller blades. The digital distribution curves of gas holdup with dimensionless radius based on the CT images could further explain the fluctuation in changes of gas holdup distribution in detail. Gas holdup increased both with gas flow rate and impeller rotating speed, but gas flow rate had more influence on gas holdup than impeller rotating speed after critical gas dispersion state.

The Eulerian–Eulerian two-fluid model coupling with the bubbles' coalescence and break-up models, and drag coefficient model were established to make CFD simulation of gas holdup distributions for the gas–liquid stirred Rushton tank under different gas flow rates and impeller rotating speeds. On the whole, the CFD simulated gas holdup distributions could roughly reflect the change trends of CT measured results, although the CFD simulated gas holdup distributions were relatively smooth and little peaks of gas holdup distribution could appear. When gas flow rate increased, the CFD simulated gas holdup values became larger than the CT measured results. It suggested that the CFD models for simulating cross section gas holdup distribution in gas–liquid stirred Rushton tank at larger gas flow rate need further improvement and this work still expects in-depth research.

Nomenclature

f_B	break-up correction coefficient, its value was equal to 1.0
F_C	coalescence correction coefficient, its value was equal to $0.07\pi^4$
C_D	drag coefficient
K	turbulent kinetic energy, m^2/s^2
N	impeller rotational speed, rpm
R_{eb}	bubble Reynolds number
Q_g	gas flow rate, m^3/s
R	radial coordinate, m
u	velocity, m/s
U_{tip}	impeller tip speed, m/s
V	tank volume, m^3

Greek letters

α	volume fraction
ε	turbulent kinetic energy dissipation rate, m^2/s^3
θ	tangential coordinate
λ	Kolmogorov length scale, m
μ	viscosity, kg/ms
ρ	density, kg/m^3

Subscripts

B	break-up
C	coalescence
c	continuous phase
i	partical group i
j	partical group j
k	the phase (liquid or gas)

Acknowledgments

Thanks for the financial support from China Scholarship Council, CREL of Washington University in St. Louis (USA), Specialized Research Fund for the Doctoral Program of Higher Education of China, National Natural Science Foundation of China (20776121), Aid program for Science and Technology Innovative Research Team in Higher Educational Institutions of Hunan Province.

References

Bao, Y.Y., Chen, L., Gao, Z.M., Chen, J.F., 2010. Local void fraction and bubble size distributions in cold-gassed and hot-sparged stirred reactors. Chemical Engineering Science 65, 976–984.

Boyer, Christophe, Duquenne, Anne-Marie, Wild, Gabriel, 2002. Measuring techniques in gas–liquid and gas–liquid–solid reactors. Chemical Engineering Science 57 (16), 3185–3215.

Brucato, A., GrisaÞ, F., Montante, G., 1998. Particle drag coefficients in turbulent fluids. Chemical Engineering Science 53 (18), 3295–3314.

Chaouki, J., Larachi, F., Dudukovic, M.P., 1997. Noninvasive tomographic and velocimetric monitoring of multiphase flows. Industrial & Engineering Chemistry Research 36 (11), 4476–4503.

Chen, J.W., Kemoun, A., Al-Dahhan, Muthanna H., Dudukovic, M.P., Lee, D.J., Fan, L.S., 1999. Comparative hydrodynamics study in a bubble column using computer-automated radioactive particle tracking (CARPT)/computed tomography (CT) and particle image velocimetry (PIV). Chemical Engineering Science 54 (13,14), 2199–2207.

Dudukovic, M.P., 2002. Opaque multiphase flows: experiments and modeling. Experimental Thermal and Fluid Science 26 (6,7), 747–761.

Han, L.C., Liu, Y.J., Luo, H., 2007. Numerical simulation of gas Holdup distribution in a standard Rushton stirred tank using discrete particle method. Chinese Journal of Chemical Engineering 15 (6), 808–813.

Hristo, Hristov V., et al., 2008. A study on the two-phase flow in a stirred tank reactor agitaed by a gas-inducing turbine. Chemical Engineering Research and Design 86 (1), 75–81.

Ford, Jason J., et al., 2008. X-ray computed tomography of a gas-sparged stirred-tank reactor. Chemical Engineering Science 63, 2075–2085.

Kemoun, A., Ong, B.C., Gupta, P., Al-Dahhan, Muthanna H., Dudukovic, M.P., 2001. Gas holdup in bubble columns at elevated pressure via computed tomography. International Journal of Multiphase Flow 27 (5), 929–946.

Khopkar, A.R., Rammohan, A.R., Ranade, V.V., Dudukovic, M.P., 2005. Gas–liquid flow generated by a Rushton turbine in stirred vessel: CARPT/CT measurements and CFD simulations. Chemical Engineering Science 60, 2215–2229.

Khopkar, Avinash R., Tanguy, Philippe A., 2008. CFD simulation of gas-liquid flows in stirred vessel equipped with dual Rushton turbines: influence of parallel, merging and diverging flow configurations. Chemical Engineering Science 63, 3810–3820.

Kumar, S.B., Moslemian, D., Dudukovic, M.P., 1995. A γ-ray tomographic scanner for imaging of voidage distribution in two-phase flow systems. Flow Measurement and Instrumentation 6 (1), 61–73.

Kumar, S.B., Moslemian, D., Dudukovic, M.P., 1997. Gas holdup measurements in bubble columns using computed tomography. AIChE Journal 43 (6), 1414–1425.

Lane, G.L., Schwarz, M.P., Evans, G.M., 2002. Predicting gas-liquid flow in a mechanically stirred tank. Applied Mathematical Modelling 26, 223–235.

Lane, G.L., Schwarz, M.P., Evans, G.M., 2005. Numerical modelling of gas–liquid flow in stirred tanks. Chemical Engineering Science 60, 2203–2214.

Law, Deify, Battaglia, Francine, Heindel, Theodore J., 2008. Model validation for low and high superficial gas velocity bubble column flows. Chemical Engineering Science 46, 4605–4616.

Liao, Y.X., Dirk, L., 2009. A literature review of theoretical models for drop and bubble breakup in turbulent dispersions. Chemical Engineering Science 64, 3389–3406.

Liu, Y.J., Han, L.C., Luo, H.A., Al-Dahhan, Muthanna H., Dudukovic, M.P., 2006. Measurement of gas hold-up distribution and digital color image reconstruction for standard gas-liquid rushton stirred tank with Cs-137 γ-CT. Journal of Chemical Engineering of Chinese Universities 20 (4), 648–652.

Luo, H., Svendsen, Hallvard F., 1996. Theoretical model for drop and bubble breakup in turbulent dispersions. AIChE Journal 42, 1225–1233.

Nienow, A.W., Wisdom, D.J., Middleton, J.C., 1977. The effect of scale and geometry on flooding , recirculation, and power in gassed stirred vessels. In: Proceedings of the 2nd European Conference on Mixing. Cambridge, England F1, pp. 1–16.

Paglinanti, Alessandro, Pintus, Sandro, Giona, Massimiliano, 2000. Time-series analysis approach for the identification of flooding/loading transition in gas–liquid stirred tank reactors. Chemical Engineering Science 55 (23), 5793–5802.

Prince, M.J., Blanch, H.W., 1990. Bubble coalescence and break-up in air-sparged bubble columns. AIChE Journal 36, 1485–1499.

Rammohan, Aravind R., 2002. Characterization of Single and Multiphase Flows in Stirred Tank Reactors. Ph.D Thesis. Washington University, St. Louis 194, 172pp.

Ranade, V.V., Deshpande, VaibhavR., 1999. Gas–liquid flow in stirred reactors: trailing vortices and gas accumulation behind impeller blades. Chemical Engineering Science 54, 2305–2315.

Ranade, V.V., Perrard, M., Xuereb, C., Le Sauze, N., Bertrand, J., 2001. Influence of gas flow rate on the structure of trailing vortices of a Rushton turbine PIV Measurements and CFD simulations. Chemical Engineering Research and Design 79 (8), 957–964.

Venneker, B.C.H., et al., 2002. Population balance modeling of aerated stirred vessels based on CFD. AIChE Journal 48 (4), 673–685.

Wang, W.J., 2002. Numerical Simulation and Experimental Investigation on Gas-Liquid Flow in a Stirred Tank. Ph.D. Thesis. Institute of Process Engineering, Chinese Academy of Sciences, China.

Wang, W.J., Mao, Z.S., Yang, C., 2006. Experimental and numerical investigation on gas–liquid flow in a Rushton impeller stirred tank. Industrial & Engineering Chemistry Research 45 (3), 1141–1151.

Zhang, Q.H., et al., 2009. Experimental determination and numerical simulation of mixing time in a gas–liquid stirred tank. Chemical Engineering Science 64, 2926–2933.